Biochemistry

pubs.acs.org/biochemistry Article

Rapid Kinetics of Pistol Ribozyme: Insights into Limits to RNA Catalysis

Suhyun Yoon, Edward Ollie, Darrin M. York, Joseph A. Piccirilli, and Michael E. Harris*

Cite This: *Biochemistry* 2023, 62, 2079−2092 Read Online

ACCESS | Metrics & More | Article Recommendations

ABSTRACT: Pistol ribozyme (Psr) is a distinct class of small endonucleolytic ribozymes, which are important experimental systems for defining fundamental principles of RNA catalysis and designing valuable tools in biotechnology. High-resolution structures of Psr, extensive structure−function studies, and computation support a mechanism involving one or more catalytic guanosine nucleobases acting as a general base and divalent metal ion-bound water acting as an acid to catalyze RNA 2′-*O*-transphosphorylation. Yet, for a wide range of pH and metal ion concentrations, the rate of Psr catalysis is too fast to measure manually and the reaction steps that limit catalysis are not well understood. Here, we use stopped-flow fluorescence spectroscopy to evaluate Psr temperature dependence, solvent H/D isotope effects, and divalent metal ion affinity and specificity unconstrained by limitations due to fast kinetics. The results show that Psr catalysis is characterized by small apparent activation enthalpy and entropy changes and minimal transition state H/D fractionation, suggesting that one or more pre-equilibrium steps rather than chemistry is rate limiting. Quantitative analyses of divalent ion dependence confirm that metal aquo ion pK_a correlates with higher rates of catalysis independent of differences in ion binding affinity. However, ambiguity regarding the rate-limiting step and similar correlation with related attributes such as ionic radius and hydration free energy complicate a definitive mechanistic interpretation. These new data provide a framework for further interrogation of Psr transition state stabilization and show how thermal instability, metal ion insolubility at optimal pH, and pre-equilibrium steps such as ion binding and folding limit the catalytic power of Psr suggesting potential strategies for further optimization.

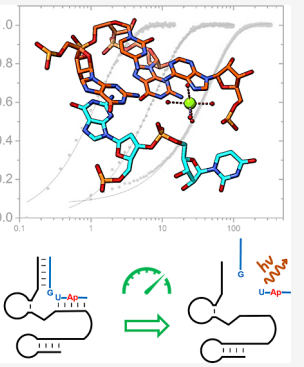

INTRODUCTION

Small ribozymes are key experimental systems for exploring the basic principles that underlie biological catalysis, and they are important tools in biotechnology and biomedicine.[1−4] Nine classes of small endonucleolytic ribozymes are currently known that catalyze RNA 2′-*O*-transphosphorylation. All of these classes accelerate RNA strand cleavage by multiple orders of magnitude, and several characteristic organizations of active site nucleobases and metal ions have emerged from high-resolution structures, extensive biochemical analyses, and integration into recent computational simulations.[5−15] A common set of defined catalytic modes appears to be employed, offering a simplified framework for describing catalysis and enabling descriptions of mechanistic alternatives with greater precision.[9,16−18] Yet, nonenzymatic reactions follow a range of mechanistic pathways amenable to different modes of catalysis,[19−21] and different classes of ribozymes may deploy distinct combinations of catalytic strategies, forming distinct intermediates and transition states. Both nucleic acid and protein catalyze RNA 2′-*O*-transphosphorylation providing contrasting examples of active sites with very different physiochemical properties. Recent comparisons of RNA 2′-*O*-transphosphorylation catalyzed by the protein enzyme ribonuclease A and the HDV ribozyme (HDVrz) using combined quantum mechanical/molecular mechanical (QM/MM) simulations benchmarked by ^{18}O kinetic isotope effects reveal that they traverse through remarkably different transition states, underscoring the breadth of the mechanistic landscape.[22,23] To define this mechanistic landscape, there is a clear need for additional comparisons between RNA and protein catalysts that have similar or distinct active site architectures. Such detailed investigation of different RNA catalysts at a high level of mechanistic detail is essential for defining fundamental aspects of biological catalysis and providing general principles and strategies for engineering novel catalysts or ones with expanded chemical range or that respond to signaling molecules.[3,4,24,25]

Pistol ribozyme (Psr) is a class of endonucleolytic ribozyme discovered by comparative genomic analysis that shares a consensus sequence including 10 conserved nucleotides, which when mutated or modified reduce catalytic function.[26−28] The Psr secondary structure consists of helices P1, P2, and P3 and a

Received: March 20, 2023
Revised: May 24, 2023
Published: June 9, 2023

https://doi.org/10.1021/acs.biochem.3c00160
Biochemistry 2023, 62, 2079−2092

pseudoknot interaction between the loop of P1 and the P2−P3 junction (Figure 1A). The available crystal structures of Psr all

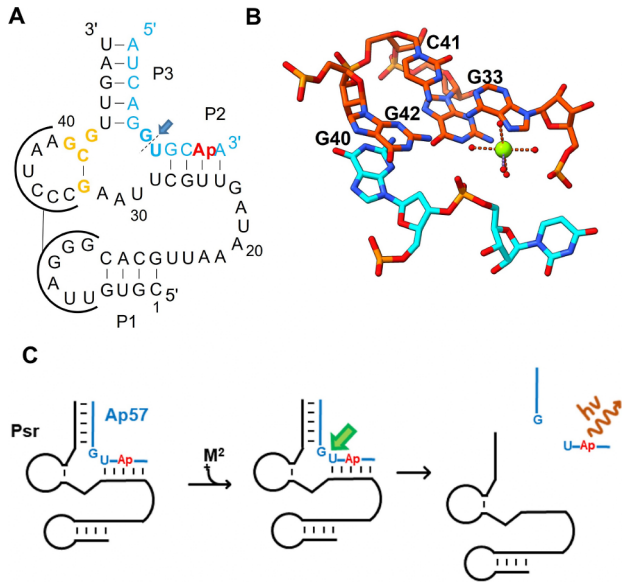

Figure 1. Pistol ribozyme (Psr) secondary structure, active site, and overall reaction scheme. (A) Secondary structure of *env*25 pistol ribozyme and substrate (A57Ap) used in this study and in previous structural and mechanistic analyses. Secondary structure adapted from reference. The cleavage site is indicated by a green arrow, and the position of the 2-aminopurine modification (Ap) is shown in red. Key active site residues G40−G42 and G33 are colored orange. (B) Three-dimensional structure of the active site of Psr based on the structure of a substrate analogue containing a deoxynucleotide substitution at the cleavage site (PDB:6UEY) with the proposed interactions with active site Mg^{2+} ion based on a vanadate transition state mimic is highlighted. The nucleotide flanking the scissile phosphate is in blue, and key active site nucleotides are shown in orange and numbered according to the secondary structure in panel A. (C) Reaction scheme for intermolecular cleavage of the short oligonucleotide substrate (A57Ap, blue) by *env*25 (black). The position of the fluorescent Ap residue is red, the cleavage site is indicated by an arrow, and the increase in Ap fluorescence upon cleavage and dissociation is depicted by a star.

show close agreement in both the overall folding of the RNA and the orientations of nucleobases in the active site adjacent to the reactive phosphoryl group.[29−32] SHAPE analysis at 37 °C shows folding of a unimolecular Psr ribozyme at a relatively low (5 mM) $MgCl_2$ concentration.[33] Compared to the absence of Mg^{2+}, divalent ions induced changes in SHAPE reactivity consistent with folding of J1/2 and nucleotides flanking the central pseudoknot. However, in the absence of Mg^{2+}, Psr remains active in high concentrations of monovalent sodium and lithium ions with much slower reaction rates. The exchange-inert metal ion complex, cobalt hexamine, at 1 mM also supports impaired catalysis with an observed rate 390-fold slower than that in 1 mM Mg^{2+}, showing that Psr catalysis does not absolutely require inner-sphere contacts with a divalent metal ion.[26,32] Nonetheless, divalent ions dramatically accelerate cleavage with a rate constant at optimal pH and $MgCl_2$ concentration predicted to be > 100 min^{-1}.[26]

The Psr belongs to a class of so-called "G + M" ribozymes[9] that are believed to use a guanine general base and divalent metal ion acid for optimal activity and utilize a L-platform/L-scaffold active site architecture[18] shared with other "G + M" and "G + A" ribozymes such as the hammerhead, VS, hairpin, and twister ribozymes as well as the 8−17 DNAzyme.[34] To accomplish catalysis, Psr uses a series of catalytic modes for transition state stabilization, which for endonucleolytic ribozymes have been individually termed α−δ.[16,17] For most endonucleolytic ribozymes including Psr, the available structural and biochemical data provide detailed models of the modes employed and the functional groups involved.[3,5,6,9,11,35] X-ray structures are available for the pre-catalytic conformation of Psr in which the nucleophilic 2′OH is replaced by H,[29,30,32] a vanadate transition state mimic at the reactive phosphate, and the cleaved product.[31] These structures show the same overall active site geometry (Figure 1B), in which interactions with the nucleobases flanking the cleavage site position the 2′-OH nucleophile for in-line attack on the scissile phosphate (α catalysis). G40 or nearby G42 may be involved in facilitating 2′OH deprotonation (γ catalysis).[32,36] Importantly, both structural and biochemical data indicate that a catalytic Mg^{2+} ion makes inner-sphere contact with G33:N7 and outer-sphere coordination to the pro-*R*p oxygen of the scissile phosphate that may provide electrostatic stabilization (β catalysis). Neutralization of the developing charge on the 5′O leaving group is proposed to be conducted by a water molecule coordinated with the active site Mg^{2+} *via* proton transfer (δ catalysis).[14]

The effects of atomic substitutions used to probe Psr active site interactions are generally consistent with the model described above, although a definitive mechanism remains unclear.[26,31,32,37] The determination of transition state interactions from ground state conformations can be challenging for small ribozymes, particularly in light of the dynamic nature of nucleic acid active sites. For many ribozyme systems, the active state capable of catalyzing chemistry is not the ground state, but rather a transient state characterized by changes in local conformation, metal ion binding mode, and protonation events. Additionally, changes in rate-limiting step, kinetic ambiguity, alternative reaction channels under different conditions, and effects of modifications on conformational dynamics can further complicate mechanistic interpretations.

An important observation regarding the role of divalent ions in catalysis comes from the observation of a log-linear correlation between Psr reaction rate and the known pK_a of the divalent metal ion supplied in the reaction.[32,38] However, the affinity of activating metal ions for Psr and their contribution to the intrinsic rate of catalysis are as yet not well defined, in part due to technical limitations. Initial biochemical characterization of Psr demonstrated that its catalytic rate is too fast to measure manually at optimal concentrations of Mg^{2+} and pH.[26] Accordingly, subsequent experiments have primarily used suboptimal concentrations of divalent metal ions and low pH to slow catalysis. This constraint restricts the ability to uncover relationships between activity and the physical properties of the system components, which obscures functional linkages upon which mechanistic interpretations can be based. As a result, important outstanding questions remain unanswered, including details about the primary catalytic mode and possible secondary modes that proceed through different pathways and might become favorable for different ribozyme variants or under different environmental conditions. These details include the number of protons transferred in the transition state, the functional groups that donate and accept those protons, and the

https://doi.org/10.1021/acs.biochem.3c00160
Biochemistry 2023, 62, 2079−2092

relationship of these events to the identity and binding mode of the divalent metal ion.

Here, we adopt a stopped-flow fluorescence spectroscopy assay, previously developed by Micura and colleagues,[2−4] to define the activation energy parameters, role of essential divalent metal ions, and proton transfer steps of Psr catalysis. Together, these new data demonstrate a high-affinity divalent ion binding with low selectivity that is essential for optimal catalysis and reveal weaker inhibitory interactions that are divalent metal ion-specific. Rapid kinetics measurements and metal titration studies permit the rate of Psr catalysis to be estimated for a series of different divalent ions in the active site. The results confirm an inverse correlation with metal aquo ion pK_a and the rate of cleavage, which is consistent with charge buildup on a metal ligand en route to the rate-limiting transition state. However, the interrelationship between ion radius, hydration free energy, and pK_a limits a direct connection between acidity and catalytic mechanism. The pL (L = H or D) dependence of Psr catalysis in H_2O and D_2O is consistent with equilibrium isotope effects (EIEs) that affect an active site acid and base in the ground state but reveal minimal contribution from proton transfers in the rate-limiting transition state.

MATERIALS AND METHODS

Preparation of Ribozyme and Substrate RNAs. All stock solutions and enzyme reactions were prepared using ultrapure deionized water and analytical grade reagents. The intermolecular form of the *env*25 (environmental sample 25) Psr ribozyme (47 nt, MW 15,301 g/mol) was generated by in vitro transcription with T7 RNA polymerase using a double-stranded PCR DNA template. The PCR template was synthesized in multiple[4−8] reactions of 100 μL containing 0.2 mM dNTPs, 5 units/μL Taq DNA polymerase (NEB), 1× reaction buffer supplied by the manufacturer, 1 μM each Prz_F and Prz_R primers, and a template oligonucleotide with the following sequences:

DNA template (MW = 19,982 g/mol)

5′ ATC AAC GCT TAG GGC TTA AGC AAC TAT TTA ACG TGG CCC TAA CCA CGC TAT AGT GAG TCG TAT TA 3′

Prz_F (MW = 6085 g/mol)

5′ TAA TAC GAC TCA CTA TAG CG 3′

Prz_R (MW = 4633 g/mol)

5′ ATC AAC GCT TCG GGC 3′

Reactions were denatured at 95 °C for 2 min followed by 30 cycles of 95 °C for 30 s; 51.8 °C for 30 s; 72 °C for 60 s; and a final incubation at 72 °C for 5 min. The PCR products were recovered by ethanol precipitation after extraction with 50:50 phenol/chloroform and chloroform. Individual in vitro transcription reactions of 400 μL contained 5 mM each of ATP, CTP, UTP, and GTP; 0.01 U/μL yeast pyrophosphatase; 26 mM $MgCl_2$, ca. 2.5 μM PCR DNA template, and optimized concentrations of T7 RNA polymerase purified in house. Reactions were incubated at 37 °C for 3−5 h, and the products were recovered by ethanol precipitation after extraction with 50:50 phenol/chloroform and chloroform. The full-length RNA transcripts were purified by both size exclusion chromatography and gel purification. For gel purification, RNAs were isolated on 8% acrylamide gels containing 4 M urea run in 1× TBE buffer, eluted into a volume of 10 mM Tris-HCl pH 7.0, 5 mM EDTA, 1% SDS estimated to be greater than five times the excised gel, and ethanol precipitation after extraction with 50:50 phenol/chloroform and chloroform. Products from in vitro transcription were also purified by chromatography on a HiLoad Superdex 16−600 75 pg column (Cytiva) running buffer in 10 mM Tris-HCl, 1 mM EDTA at a flow rate of 1 mL/min.

The 11 nt substrates with 2-aminopurine substitution (A57Ap; 3732 g/mol) and containing both Ap modification and 2′-deoxy modification at the cleavage site (dA57Ap; 3716 g/mol) were obtained commercially (Horizon):

A57Ap—A.U.C.A.G.G.U.G.C.2Ap.A

dA57Ap—A.U.C.A.G.dG.U.G.C.2Ap.A

RNAs were deprotected according to the manufacturer's instructions. The absorbance at 260 nm of ribozyme and substrates was measured, and concentrations were determined using the following extinction coefficients ε (M^{-1} cm^{-1}) = 469,400 for native Psr and 106,900 for A57Ap and dA57Ap.

Steady-State Fluorescence and Circular Dichroism Spectroscopy. For analysis of the effect of 2-aminopurine fluorescence in the substrate upon binding to the Psr ribozyme, we used the inactive dA57Ap substrate analogue bearing a 2′-deoxynucleotide at the cleavage site. Samples of dA57Ap, Psr, and their complexes (1:0.25−1:2) were prepared in 500 μL containing 1 μM dA57Ap and 0−2 μM Psr in 30 mM HEPES pH 8.0, 2 M NaCl, 0.5 mM EDTA. Samples were heated to 85 °C for 5 min and then transferred to 25 °C and incubated for an additional 10 min before the addition of 5 mM $MgCl_2$. Spectra were acquired using a Cary Eclipse fluorescence spectrometer. Scans were taken in a 5 mm × 5 mm thermostated cuvette at 25 °C from 320 to 450 nm with an excitation wavelength of 305 nm and excitation and emission slits at 5 nm, and a scan rate of 120 nm/min. Three individual spectra were averaged, and an averaged spectrum of a background control was subtracted. To evaluate the apparent affinity and stoichiometry of ES complex formation in the absence of Mg^{2+}, the intensity of the fluorescence at 265 nm (F) versus increasing [E] was plotted and fit to eq 1.

$$F = \Delta F\left(1 - \frac{([S] + [E] + K) - \sqrt{([S] + [E] + K)^2 - 4[E][S]}}{2}\right) + C \quad (1)$$

ΔF is the change in the fluorescence intensity, [S] is the substrate concentration, and K is the apparent equilibrium dissociation constant in units of [E] and [S]. The effect of addition of 5 mM $MgCl_2$ on the spectrum of the ES complex was analyzed by creating reaction containing either 1 μM A57Ap substrate alone or bound to an equivalent concentration of Psr. After acquisition of the spectrum for the ES complex, 5 μL of a 0.5 M solution of $MgCl_2$ was added to bring the final concentration to 5 mM. The spectrum of the sample (designated EP) was reacquired after a 1 min incubation at 25 °C.

CD spectra were collected on an Applied Photophysics Chirascan spectrometer. Spectra were collected from 200 to 320 nm in a 5 mm quartz cuvette at 0.2 nm increments. The sample size was set to 500 with an error of ±0.0001 and a sample period of 25 μs. The entrance and exit slits were 1 nm. Thermal melts were monitored at 265 nm from 15 to 85 °C, and the temperature of the sample was recorded using an

https://doi.org/10.1021/acs.biochem.3c00160
Biochemistry 2023, 62, 2079−2092

internal probe. An equilibration time of 5 min at each temperature was used throughout the experiment. The T_m for Psr was determined by fitting the data to the following function

$$\text{mdeg} = \frac{(m_f T + b_f) + (m_u T + b_u) e^{(\Delta H/R)\left(\frac{1}{(T_m+273.15)} - \frac{1}{(T+273.15)}\right)}}{1 + e^{(\Delta H/R)\left(\frac{1}{(T_m+273.15)} - \frac{1}{(T+273.15)}\right)}} \quad (2)$$

where mdeg is the CD signal at a given temperature, m_f and m_u are the slopes of the upper (folded) and bottom (unfolded) baselines, respectively, b_u and b_f are the y-intercepts of the folded and unfolded baselines, respectively, ΔH (kcal mol^{-1}) is the folding enthalpy, and T_M (°C) is the melting temperature, and R is the gas constant (0.001987 kcal K^{-1} mol^{-1}).[39]

Kinetic Analysis of Psr Using Stopped Flow Fluorescence. The time dependence of changes in the fluorescence of 2-aminopurine positioned at A57 in the A57Ap substrate was measured by stopped-flow fluorescence spectroscopy using an Applied Photophysics SX20 LED instrument equipped with a 300 nm monochromatic LED light source in a single mixing (two syringe) mode. Fluorescence was recorded with photomultiplier voltage settings of 7−8 mV to optimize sensitivity. Detector voltage signal was converted to arbitrary units to facilitate comparison of kinetic traces. Power supply outputs were varied between 2 and 12 mA depending on the duration of the kinetics to optimize sensitivity and minimize photobleaching. Photobleaching for reactions was evaluated by comparing rate constants obtained at different LED outputs. Emission was measured at wavelengths >320 nm using a cut-on filter (Edmond Optics). Temperature was maintained at 25 °C using a circulating water bath connected to the sample handling unit. Solutions containing pre-annealed Psr in complex with the A57Ap substrate at 2× the desired concentrations of 1.5 and 1 μM were mixed with reaction buffer containing a 2× concentration of the target concentration using a total drive volume of 140 μL.

The fluorescence time courses $F(t)$ were fit to a single exponential to obtain the fluorescence amplitude and the observed rate constant for each phase where $F(0)$ is the initial fluorescence and t is the time

$$F(t) = F(0) + Ae^{-k_{obs}t} \quad (3)$$

The dependence of the k_{obs} for Psr as a function of divalent metal ion concentration was analyzed using an equation for a single metal ion or class of ion binding sites that is essential for catalysis associates under equilibrium conditions with apparent K_{MA} and a cleavage rate constant k_c. The second independent and noninteracting site that binds with weaker affinity and a dissociation constant K_{MB} results in inhibition of catalytic function

$$k_{obs} = \frac{k_c}{1 + \frac{K_{MA}}{[M]} + \frac{[M]}{K_{MB}}} \quad (4)$$

The dependence of k_{obs} on Ca^{2+} concentration did not fit to eq 4 and was analyzed by using a general binding model that accounts for non-cooperative, cooperative, or anti-cooperative binding modes.

$$k_{obs} = \frac{k_c}{1 + \frac{(K_d)^n}{[M]^n}} \quad (5)$$

The dashed line in Figure 7B represents a fit to the data with n = 1 (non-cooperative). The solid line shows unconstrained fitting yielding values of n = 0.54 (anti-cooperative; n < 1) and K_d = 150 mM.

The temperature dependence of Psr catalysis was analyzed using Eyring transition state theory. A plot of $\ln(k_{obs}/T)$ versus $1/T$ was fit to eq 6 to obtain the values for the apparent activation enthalpy ($\Delta H^{\ddagger}_{app}$) and entropy ($\Delta S^{\ddagger}_{app}$).

$$\ln\left(\frac{k_{obs}}{T}\right) = \frac{-\Delta H^{\ddagger}_{app}}{RT} + \frac{\Delta S^{\ddagger}_{app}}{R} + \ln\frac{k_B}{h} \quad (6)$$

In eq 6, T is the absolute temperature, R is the gas constant 8.314 J mol^{-1} K^{-1}, k_B is the Boltzmann constant 1.38 × 10^{-23} J K^{-1}), and h is Planck's constant (6.626 × 10^{-34} J s).

Solvent Kinetic Isotope Effects. Deuterium oxide (D_2O) (D, 99.9%) (Cambridge Isotope Laboratories) was used for all sample preparations that involve D_2O. Buffers used were MOPS for pL 7.5, TAPS for pL 8, 8.25, 8.5, 8.75, and 9, and CHES for pL 9.25 and 9.5 (Research Products International). Salts and reaction buffers were dissolved in deionized filtered water or D_2O. The pH meter was calibrated at 25 °C and readings for buffers and solutions were measured at 25 °C; for solutions using D_2O, the pD was determined by adding 0.4 to the pH reading. The effect of 2 M NaCl on pH meter response using the calibration curve for Na^+-containing solutions from Chadalavada *et al.*[40] Stopped-flow kinetics experiments for measurement of D_2O effects were performed essentially as described, above. The observed rate constants were plotted as a function of pH or pD accordingly and fit to a general equation for two ionizable active site groups acting as acid and base.[41]

$$k_{obs} = \frac{k_c}{1 + 10^{(pK_{a,B} - pH)} + 10^{(pK_{a,B} - pK_{a,A})} + 10^{(pH - pK_{a,A})}} \quad (7)$$

The pK_a values of the acid and base are designated p$K_{a,A}$ and p$K_{a,B}$, respectively, and k_c is the intrinsic cleavage rate.

RESULTS

Analysis of Psr Kinetics by Stopped-Flow Fluorescence Spectrometry. To investigate Psr kinetics, we used a fluorescence-based assay developed by Micura and colleagues that consists of a 16 nucleotide substrate, A57Ap, containing a 2-aminopurine (2Ap) nucleobase that anneals to the 32 nucleotide *env25* Psr (Figure 1C).[29,31,37,42] The reaction is initiated by mixing the pre-annealed complex with divalent metal ions, and product formation is quantified by monitoring the increase in 2Ap fluorescence upon cleavage and product dissociation (Scheme 1).[29,31,37] This method has provided a highly valuable tool to establish Psr structure−function relationships and importantly enables analysis of rapid kinetics.

We demonstrated the formation of an equimolar complex of Psr (E) and A57Ap (S) under the conditions used in subsequent kinetic experiments by titrating increasing concentrations of E into a fixed concentration (1 μM) of S in the absence of divalent metal ion in 30 mM HEPES pH 8, 2

Scheme 1

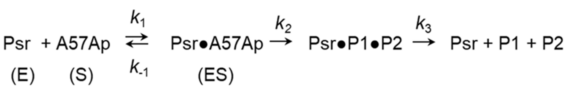

https://doi.org/10.1021/acs.biochem.3c00160
Biochemistry 2023, 62, 2079−2092

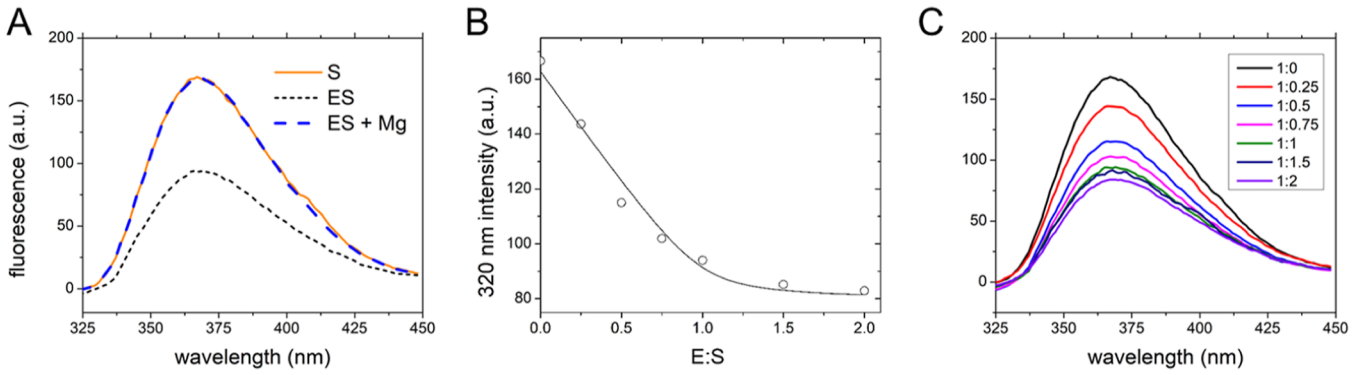

Figure 2. Steady-state fluorescence of Psr S and ES complexes. (A) Emission spectra of 1 μM A57Ap substrate oligonucleotide in the presence of increasing concentrations of *env*25 Psr (E) (λ_{ex} = 305 nm). (B) Dependence of fluorescence intensity at λ_{max} = 360 nm on the E/S ratio. Individual data points are shown as circles; the line shows a fit to the quadratic form of the equilibrium binding equation. (C) Emission spectra of S (solid orange line), E/S (dotted black line), and the E/S complex after addition of Mg^{2+} (blue dashed line).

M NaCl, 0.05 mM EDTA. High monovalent ion concentrations are used to fulfill diffuse ion interactions involved in RNA folding allowing easier characterization of site-specific binding by divalent ions essential for catalysis.[43] ES complex formation was quantified by the decrease in 2Ap fluorescence as a function of E/S ratio (Figure 2A,B); the data were fit to an equation for stoichiometric binding (eq 1) and are consistent with a stoichiometry of 1:1 and an approximate $K_{d,app}$ of < 0.1 μM. As expected, the emission spectrum of 1 μM A57Ap undergoes a large decrease in fluorescence due to Psr binding and the spectrum returns to the intensity of the free S upon incubation for 5 min after addition of Mg^{2+} (Figure 2C).

Next, we used stopped-flow spectroscopy to measure the time-dependent changes in the fluorescence intensity upon mixing preformed ES complex with buffer containing Mg^{2+} at 25 °C (pH 8.0, 2 M NaCl and 5 mM $MgCl_2$). The resulting data demonstrated an increase in signal intensity upon mixing, consistent with substrate cleavage and product release. The expected k_{off} for the 4 nucleotide cleavage products is ~100 s^{-1} based on recent analyses of RNA association and dissociation kinetics.[44] This is significantly faster than the fastest rate constants (1 s^{-1}) we measure for Psr under the conditions employed in this study. No increase in fluorescence intensity was observed when the ES complex was mixed with buffer lacking Mg^{2+} (Figure 3A). We confirmed that the change in fluorescence was due to product formation by analyzing fluorescence of an A57Ap substrate containing a 2′-deoxy modification at the cleavage site (dA57Ap). The ES complex with dA57Ap in the presence of Mg^{2+} gives the same quenched fluorescence signal as the ES complex with A57Ap in the absence of Mg^{2+}, consistent with the modification blocking catalysis, but not binding (Figure 3B). These findings provide no evidence for significant conformational changes or refolding of the ES complex upon addition of Mg^{2+}; however, we cannot rule out the possibility of a conformational change that depends on the presence of the 2′OH or does not alter the environment of the 2Ap probe. The data for the Psr and A57Ap substrate reaction were fit to a single exponential function (eq 3), and the observed rate constant (k_{obs}) at 1 mM Mg^{2+} of 0.14 ± 0.05 s^{-1} is similar to the value of 0.163 s^{-1}, determined manually under these conditions by using gel electrophoresis to quantify product formation.[32] Importantly, as shown, below, the dependence of the observed rate constant measured by stopped flow on pH and metal ion type also

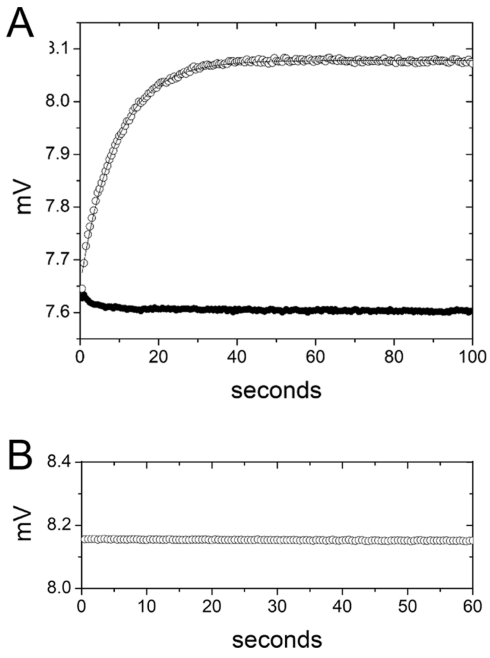

Figure 3. Stopped-flow fluorescence analysis of Psr reaction kinetics. (A) Time-dependent change in A57Ap fluorescence upon mixing Psr/A57Ap and Mg^{2+} to achieve a final concentration of 1 μM A57Ap, 1.5 μM Psr, and 1 mM Mg^{2+} (open circles) or mixing with buffer without Mg^{2+} (filled circles). The solutions mixed in the flow cell were excited using a 300 nm LED source and total fluorescence detected using a 320 nm high pass filter. (B) Time-dependent Ap fluorescent signal after mixing of 1 μM (final concentration) E/dA57Ap complex, in which the cleavage site contains a 2′-deoxy modification, with Mg^{2+} to achieve a final concentration of 1 mM.

matches previous results using gel-based assays, further establishing the approach.

Characterization of Psr Thermal Stability and Reaction Temperature Dependence. To evaluate the range of temperatures accessible for kinetic studies, circular dichroism (CD) spectroscopy was used to analyze the thermal stability of the Psr ES complex. The CD spectra of Psr and Psr complexed to dA57Ap have essentially identical CD spectra, showing a large positive signal at 268 nm with a shoulder of positive intensity at around 245 nm, characteristic of dsRNA (Figure 4A).[45,46] There is minimal effect of Mg^{2+} on the CD spectra of E and EdS, consistent with minimal change in the

https://doi.org/10.1021/acs.biochem.3c00160
Biochemistry 2023, 62, 2079−2092

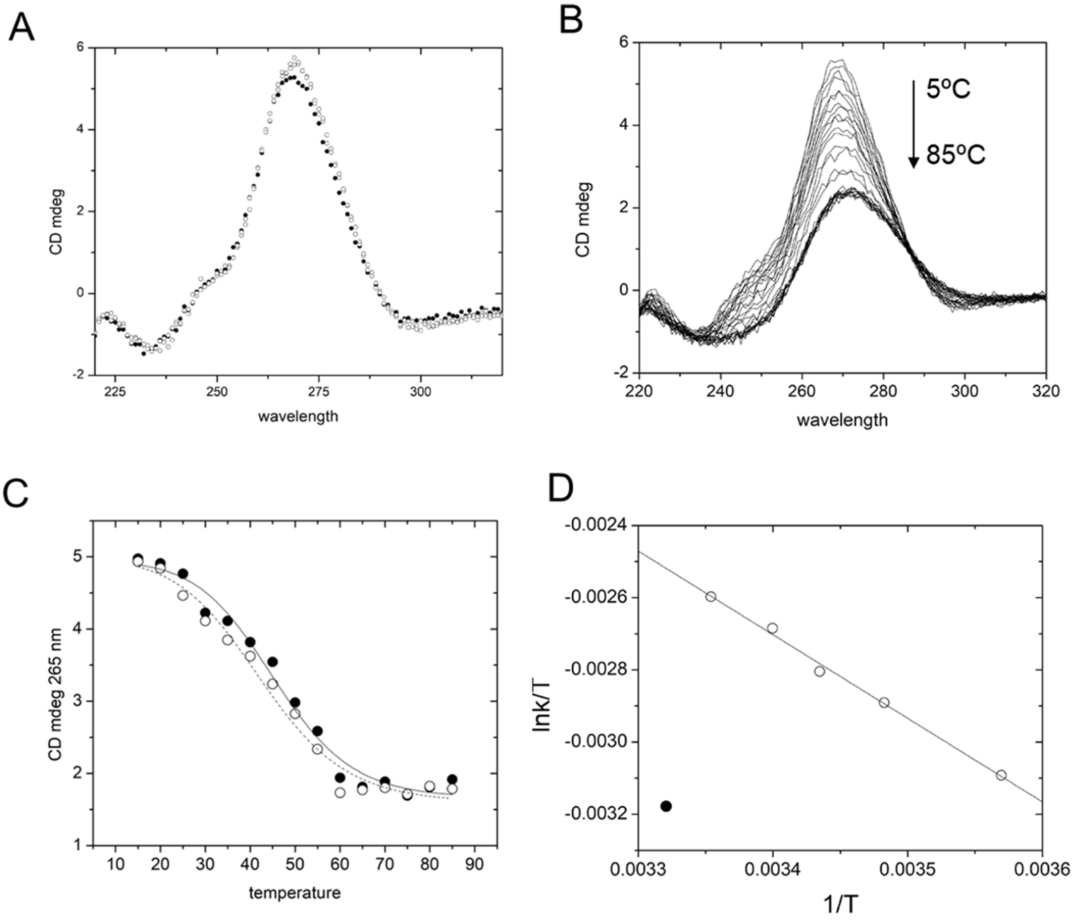

Figure 4. Temperature dependence of Psr folding and reaction kinetics. (A) CD spectra of a sample containing 1 μM dS and 1.1 μM E in 30 mM HEPES pH 8.0, 2 M NaCl, and 5 mM $MgCl_2$ (15 °C). (B) Spectra were acquired at a series of increasing temperatures and overlaid, the change in CD signal associated with thermal unfolding is indicated by an arrow. (C) Plot of CD signal intensity at 265 nm as a function of temperature (5−85 °C). The data were fit to a two-state reversible unfolding mechanism to estimate the T_m for the Psr ES (open circles) and ES complex in 5 mM Mg^{2+} (filled circles). (D) Thermodynamic analysis of Psr temperature dependence (7−25 °C). The reaction rate decreases dramatically above 25 °C as evidenced by the data point obtained at 28 °C (filled circle), which was excluded from data fitting. The temperature-dependent data (open circles) are fit to a linear equation to calculate the apparent activation energy ($\Delta H^{\ddagger}_{app}$ = 1.36 ± 0.06 kcal/mol) and entropy change ($\Delta S^{\ddagger}_{app}$ = −0.66 e.u.).

secondary structure. The CD spectra of E alone and EdS complex in buffer with and without 5 mM $MgCl_2$ were collected as a function of temperature to determine their relative stabilities. The CD signal is maximal and constant from 10 to 25 °C; however, at higher temperatures, a gradual decrease in CD intensity is observed, with a T_m of 42.4 °C in the absence of $MgCl_2$ and 45.4 °C in 5 mM $MgCl_2$, and a shift in λ_{max} to a higher wavelength (265 nm to 270 nm) (Figure 4B,C). The low temperature optimum for the intermolecular *env*25 Psr is consistent with other fragmented small ribozymes.[47]

Under conditions where the RNA retains folded structure (10−25 °C, 30 mM HEPES pH 8.0, 2 M NaCl, and 5 mM $MgCl_2$), we observe an increase in k_{obs} as temperature increases, characteristic of an endothermic reaction. The observed rate constant drops precipitously above 25 °C (Figure 4C), consistent with thermal unfolding as demonstrated by CD. Kinetic data collected below 25 °C were analyzed using an Eyring plot of $\ln(k_{obs})/T$ versus $1/T$ (Figure 4D). The data fit a linear function (eq 6), and the resulting slope and intercept indicate an apparent activation enthalpy ($\Delta H^{\ddagger}_{app}$) of 1.36 ± 0.06 kcal/mol and apparent enthalpy change ($\Delta S^{\ddagger}_{app}$) of −0.66 e.u. These parameters are significantly smaller than those measured for other small endonucleolytic ribozymes and DNAzymes, which have $\Delta H^{\ddagger}_{app}$ similar to 29 kcal/mol described for nonenzymatic RNA 2′-*O*-transphosphorylation catalyzed by base.[48−50] Possibly, the pre-catalytic equilibria associated with Psr cleavage have offsetting contributions to $\Delta H^{\ddagger}_{app}$.[49,51] Nonetheless, the fact that Psr is an outlier with respect to enthalpy and entropy of activation compared to other small endonucleolytic nucleic acids reveals a basic difference in its biophysics and may reflect a different rate-limiting step.

Analysis of Proton Transfer Using Solvent D_2O Kinetic Isotope Effects. Analysis of solvent D_2O kinetic isotope effects (SKIEs) can provide information on protons transferred in the transition state, solvation, and changes in rate-limiting step.[52−54] Proton transfer in the transition state gives rise to deuterium isotope effects (ϕ^{TS}) that are normal ($k_H/k_D > 1$).[52] Because they are expressed in the transition state, they contribute to the observed SKIE at all pL values. However, there are also significant EIEs on the speciation of ionizable functional groups involved in catalysis that are reflected in an increase in their apparent pK_a values. Depending on whether the affected functional group acts in its protonated or deprotonated form (e.g., as an acid or base),

https://doi.org/10.1021/acs.biochem.3c00160
Biochemistry 2023, 62, 2079−2092

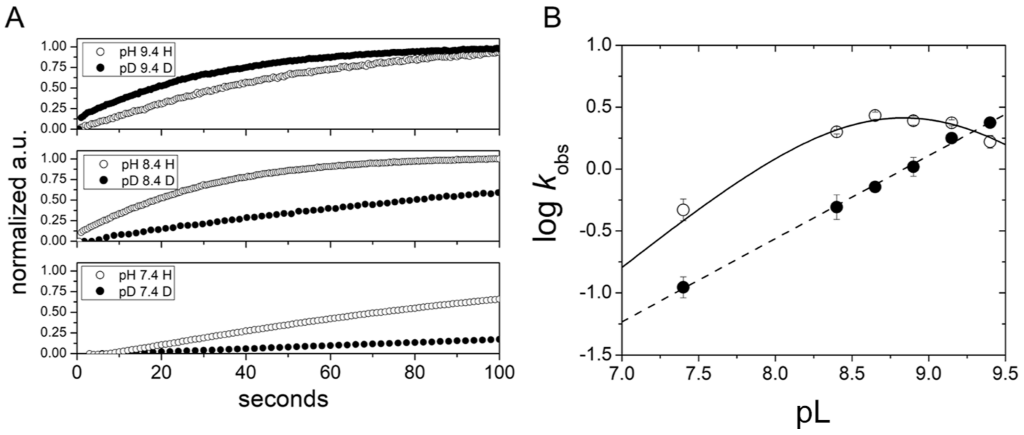

Figure 5. Analysis of solvent kinetic isotope effects on Psr reaction kinetics. (A) Time-dependent change in 2Ap fluorescence upon mixing ES and Mg^{2+} to achieve a final concentration of 1 μM S, 1.5 μM E at pL (L = H or D) 9.4, 8.4, and 7.4 run in H_2O (open symbols) or D_2O (filled symbols). (B) pL profiles of log(k_{obs}) for Psr in H_2O (open symbols) and D_2O (filled symbols) are shown. The solid and dashed lines represent fits to the H_2O and D_2O data, respectively, to a model for an enzyme with active site acid and base with pK_a values p$K_{a,A}$ and p$K_{a,B}$, respectively (eq 7).

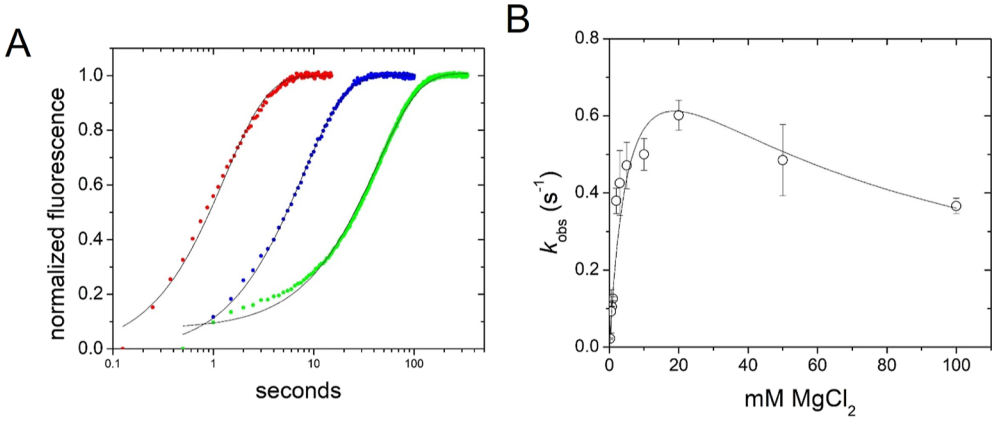

Figure 6. Mg^{2+} concentration dependence of Psr cleavage rate constant under conditions of 30 mM HEPES pH 8.0, 2 M NaCl and increasing concentrations of divalent metal ion. (A) Time-dependent changes in fluorescence of Psr ES complex mixed with $MgCl_2$ containing buffer to achieve a final concentration of 0.2 mM (red points), 2 mM (blue points), or 20 mM (green points). (B) Dependence of k_{obs} (circles) on Mg^{2+} concentration. The data are fit to an equation for equilibrium binding of two independent, non-interacting metal ion binding sites that include an activating ion M_A and an ion that inhibits catalysis M_B as depicted in the mechanism shown in Scheme 2.

the increase in pK_a will result in an increase or decrease in the fraction of active enzyme. This effect is typically visualized as a shift in the pL vs rate profile to higher pL values in D_2O, while the effect on proton transfer in the transition state ϕ^{TS} results in a decrease in k_{obs} that is independent of pL. Importantly, the observed SKIE will necessarily be a function of both EIE and ϕ^{TS} values, and their relative contributions and magnitudes will dictate whether the overall effects are normal or inverse.[54]

To estimate the EIEs on active site functional groups and any fractionation due to ϕ^{TS} effects, we compared the pL versus k_{obs} profile for Psr in H_2O and D_2O in buffer containing limiting (1 mM) $MgCl_2$ at 25 °C (Figure 5). The data were fit to a simple equilibrium mechanism for acid/base catalysis (eq 7). Calculated p$K_{a,A}$ and p$K_{a,B}$ based on the pH rate profile were 8.5 and 9.1 for Psr in H_2O, respectively. The pD rate profile was shifted to higher pL values due to the inverse EIEs resulting in a linear relationship between pD and log(k_{obs}) over the range tested. The maximum rate constant in D_2O appears at least as fast as in H_2O, implying that isotopic substitution has very little effect on the rate-limiting transition state. The active site functional group designated p$K_{a,A}$ appears to undergo an increase of >0.5 units. Indeed, over the narrow range of pL tested, the observed solvent isotope effect transitions from normal to inverse effects at high pL. These data are consistent with large EIEs that result in increases in the pK_as of active site functional groups in D_2O and only a small, if any, contribution from proton transfer in the rate-limiting transition state.

Psr Divalent Metal Ion Dependence. To quantify the activation of Psr catalysis by divalent metal ions, we determined k_{obs} at optimal pH in Mg^{2+} and high monovalent ion conditions (2 M, 25 °C, pH 8.0) at 0.2−100 mM Mg^{2+} (Figure 6). The data fit a single exponential function over the range of Mg^{2+} concentrations tested, and k_{obs} is observed to increase linearly below 10 mM but saturates and decreases above 20 mM. These data are consistent with an equilibrium model in which high affinity metal binding activates catalysis (M_A), while a second inhibitory metal ion binding site with lower affinity blocks product formation (M_B) (Scheme 2). The dependence of k_{obs} on Mg^{2+} concentration fits an equation for this mechanism that assumes independent non-cooperative, equilibrium binding of the two classes of ions (eq 4). The apparent Hill slope for binding of the activating ion is unity,

https://doi.org/10.1021/acs.biochem.3c00160
Biochemistry 2023, 62, 2079−2092

Scheme 2

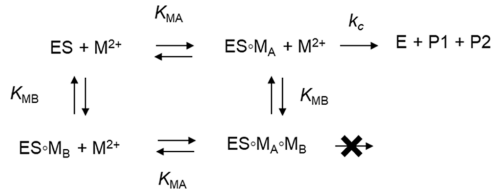

consistent with a single site or class of sites that contribute to catalysis.

Previous experiments using the *env*25 Psr showed a linear inverse correlation between the pK_a of the divalent metal ion hydrate and the log of the observed rate constant, consistent with a role as an active site acid.[32] Recent detailed biochemical characterization of the Psr from the bacterium *Paenibacillus polymyxa* further confirmed the quantitative relationship between cleavage activity and pK_a of a hydrated metal ion.[38] However, this analysis used observed rate constants derived from experiments conducted at low pH (pH 6) that were not adjusted to account for the degree of metal ion occupancy at the catalytic and inhibitory binding sites. Differences in the rate-limiting step for reactions involving different metal ions could also confound a simple mechanistic interpretation. Previous studies omitted Cd^{2+} and Zn^{2+}, which have relatively low pK_a, because the rates were too fast to measure manually or because the observed values were identified as statistical outliers compared to the values obtained for reactions in the presence of other divalents.

Accordingly, we revisited the metal ion dependence of Prs using stopped-flow methods to avoid constraints due to rapid kinetics. Before attempting to correlate rate with the pK_a of metal bound water, we determined the dependence of rate on metal ion concentration for each metal ion, allowing deconvolution of metal ion binding versus catalysis. We analyzed the rate constant in Ca^{2+} (pK_a = 12.8) Mg^{2+} (11.4), Mn^{2+} (10.59), Co^{2+} (9.85), Cd^{2+} (9.1), and Zn^{2+} (8.96). Apparent rate constants were measured and plotted as a function of metal ion concentration (Figure 7A–F). Data were fit to the equilibrium binding model (Scheme 2; eq 4) used to analyze Mg^{2+} binding and activation of catalysis to estimate K_{MA}, K_{MB}, and k_c (Table 1). The metal ions tested bind with apparent affinities of 0.2–16 mM; the weakest are Mg^{2+} and Cd^{2+} with K_{MA} of 6 mM and 16 mM, respectively. Zn^{2+} possesses the highest affinity (0.21 mM) and the fastest observed k_c (1.2 s^{-1}, pH 6.0). All the ions tested except Ca^{2+} show inhibition at higher ion concentrations with similar K_{MB} of ca. 50–90 mM. While the origin of the inhibitory effects is not known, they may represent interactions that are unimportant for the physiological function of the ribozyme given their low affinity and the fact that they are observed at very high ionic strength conditions. However, they are important to account for in estimating an accurate value of k_c. The dependence of k_{obs} on Ca^{2+} concentration is distinct as it does not show inhibition at higher concentration over the concentration range tested (Figure 7B). The data for Ca^{2+} as the divalent ion also do not follow a model for binding of a single activating ion, rather, the data are well-described by an anti-cooperative binding of two ions (eq 5) ($n_{Hill} \sim 0.5$).

Fitting the titration data for each divalent metal ion to the mechanism shown in Scheme 2 provides an estimate of k_c that attempts to account for the overlapping contributions from binding of M_A and M_B to k_{obs}. Nonetheless, these overlapping titrations will impact accuracy, especially when the M_A and M_B sites have similar metal ion binding affinities as in the case of Cd^{2+}, where the difference between $K_{d,MA}$ and $K_{d,MB}$ is ca. 4-

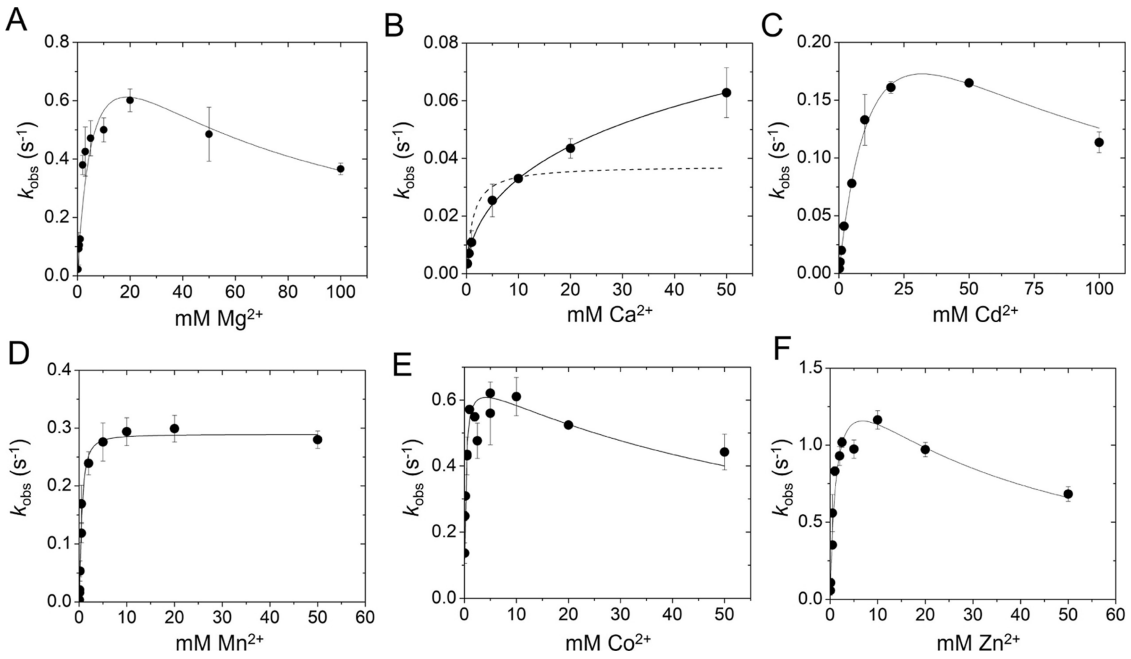

Figure 7. Comparison of the divalent metal ion dependence of Psr. (A–F) Plot of k_{obs} determined by stopped-flow fluorescence versus concentration for (A) Mg^{2+}, (B) Ca^{2+}, (C) Cd^{2+}, (D) Mn^{2+}, (E) Co^{2+}, and (F) Zn^{2+}. Data were collected at pH 6.0 for all ions except Mg^{2+} and Ca^{2+} (data collected at pH 8.0). Titration data for Mg^{2+}, Cd^{2+}, Co^{2+}, and Zn^{2+} are fit to a mechanism for binding of an activating (M_A) and inactivating (M_B) metal ion described in Scheme 2 (solid line). The data for reactions with Ca^{2+} are fit to a model for a single activating metal ion (dashed line) or anti-cooperative binding of two divalent ions (solid line). The data for reactions in which Mn^{2+} was the divalent ion are fit to a single site equilibrium binding model. The fitting results and errors are reported in Table 1.

https://doi.org/10.1021/acs.biochem.3c00160
Biochemistry 2023, 62, 2079–2092

Table 1. Observed Divalent Ion Binding Affinities and Catalytic Rate Constants

	pK_a	K_{MA} (mM)	K_{MB} (mM)	k_c (pH 8.0) (s^{-1})	k_c (pH 6.0) (s^{-1})	k_c/K_M (M^{-1} s^{-1})	k_{cat} (s^{-1})
Ca^{2+}	12.8	1.3 (3)	na	0.038		0.054[a]	0.002
Mg^{2+}	11.4	6 (2)	57 (33)	1.0 (0.3)		1.59[a]	0.047
Mn^{2+}	10.59	0.7 (2)	na		0.30 (0.01)	311.7	2.26
Co^{2+}	9.85	0.33 (0.10)	92 (44)		0.67 (0.06)	733	8.61
Cd^{2+}	9.1	16 (4)	63 (24)		0.35 (0.06)	12.2	0.097
Zn^{2+}	8.96	0.21 (0.06)	51 (34)		1.2 (0.1)	4200	16.3

[a]Extrapolated from pH 8.0; standard deviations are show in parenthesis.

fold (Table 1). We also analyzed how the identity of the metal ion affects $(k_c/K_M)^{M^{2+}}$, the second-order rate constant for the reaction of ES at low metal ion concentration. Conducting reactions under limiting ion concentrations below K_{MA} limits the contribution of inhibitory ions on the reaction rate. As $(k_c/K_M)^{M^{2+}}$ corresponds to the reaction starting from a ground state of free ES and free M^{2+} going to products, the free energy barrier will include contributions from metal ion binding, ionization equilibria, and the rate-limiting step for conversion of the complex ESM^{2+} to products. A mechanism for catalysis at limiting metal concentration that includes these potential contributions is depicted in Scheme 3, which provides a framework for better understanding their potential contributions to k_{obs}.

Scheme 3

$$ES + M^{2+} \underset{}{\overset{K_{MA}}{\rightleftharpoons}} ES{\circ}M_A^{2+} \overset{K^{\ddagger}}{\rightleftharpoons} [ES{\circ}M_A^{2+}]^{TS}$$

Scheme 3 assumes equilibrium binding of M^{2+} in the hydrated form with all bound water molecules protonated to form the catalytic species $ES^*M_A^{2+}$, which stabilizes the chemical transition state. Thus, the second-order rate constant at limiting $[M^{2+}]$ that we term k_c/K_M will be affected by all these processes. Estimation of k_c from k_c/K_M requires information on metal ion equilibrium binding affinity. Importantly, the observed value of K_{MA} determined from fitting the metal titration data is not correlated by the relative affinity of divalent ions for simple nucleotide phosphates (Figure 8A). Therefore, the selectivity of the ribozyme metal binding site for individual ions differentially influences the observed magnitude of k_c/K_M. To estimate the magnitude of k_c, this effect can be accounted for using the observed value for K_{MA}. The relative magnitudes of the values of k_c estimated from using Schemes 2 and 3 are similar and follow a linear relationship (Figure 8B). However, the magnitude of k_c estimated from k_c/K_M measured at limiting concentration is consistently higher reflecting less susceptibility to inhibitory effects from M_B and is likely to be the most accurate. The correlation between Psr catalysis and the pK_a of the divalent metal aquo ion is reproducible for k_c/K_M and for k_c estimated by using Scheme 2 or Scheme 3 (Figure 8C). The similar dependence of k_c/K_M and k_c on metal ion pK_a is consistent with minimal influence of pK_a on a metal ion's ground state binding (K_M in Scheme 3). Additionally, the $\log(k_c)$ also correlates with other divalent metal ion properties related to its effect on water coordination (Figure 8D–F). The positive charge on divalent ion attracts electron density from the water oxygen atom thereby decreasing the electron density in the OH bonds resulting in greater acidity. A similar correlation between $\log(k_c)$ and ionic radius is therefore expected since for smaller ions, shorter internuclear distances to the coordinated water molecule result in a greater effect on its electron density. Hydration free energy also depends on ion charge density which is in turn greater for smaller ions, and this parameter also correlates with $\log(k_c)$. Smaller ions with greater charge density have a higher absolute hardness, and therefore a similar correlation is expected and observed.

DISCUSSION

The application of stopped flow spectroscopy described here enables kinetic analysis of Psr catalysis unconstrained by limitations in measuring rapid reaction rates, allowing investigation of a wider range of reaction conditions. The new data both confirm and refine the current model for the overall mechanistic steps required for RNA cleavage and illuminate potential limitations in our understanding of catalytic mechanism and transition state interactions.

Psr Exhibits Anomalous Temperature Dependence. A key characteristic of the Psr construct used here, and in previous work, is its instability at higher temperatures and relative insensitivity to temperature change at temperatures below 25 °C. Surprisingly, we observe a comparatively small activation energy (1.36 kcal/mol) and small, negative entropy change (−0.66 e.u.) for Psr catalysis. The apparent activation energy parameters of Psr are significantly different from the values reported for other endonucleolytic RNA and DNA and for nonenzymatic RNA cleavage. The $\Delta H^{\ddagger}$ and $\Delta S^{\ddagger}$ for the 8−17 DNAzyme reaction associated with substrate binding and catalysis are reported as +28.7 kcal/mol and +21 e.u, respectively.[55] These values are similar to the HHrz reaction that was measured by adding Mg^{2+} to pre-annealed ES complexes ($\Delta H^{\ddagger}$ = +30.3 kcal/mol and $\Delta S^{\ddagger}$ = +36 e.u.).[49] Nonenzymatic RNA 2′-*O*-transesterification is also characterized by a large positive enthalpy of activation ($\Delta H^{\ddagger}$ = +29 kcal/mol).[48] In the case of hairpin ribozyme, docking of its two helical domains is strongly enthalpy-driven.[56] For docking of the P1 duplex substrate to the L-21 ScaI group I ribozyme, $\Delta H^{\ddagger}$ is +22 kcal/mol and also is subject to a large positive activation entropy (+21 e.u.).[57] Thus, unlike Psr, a variety of RNA reactions reflecting both conformational and chemical transitions have large activation enthalpies and can be subject to significant entropic driving forces as well.

Potential bases for the anomalous temperature effects observed for Psr could include missing functional structure in the intermolecular construct, unique features of its chemical mechanism, overlapping unfolding transitions, and alternative reaction channels. The intermolecular Psr construct characterized in these studies is a well-developed model subject to extensive structural and chemical modification studies providing an essential context for mechanistic interpretation. However, given that the flanking sequences associated with Psr

https://doi.org/10.1021/acs.biochem.3c00160
Biochemistry 2023, 62, 2079−2092

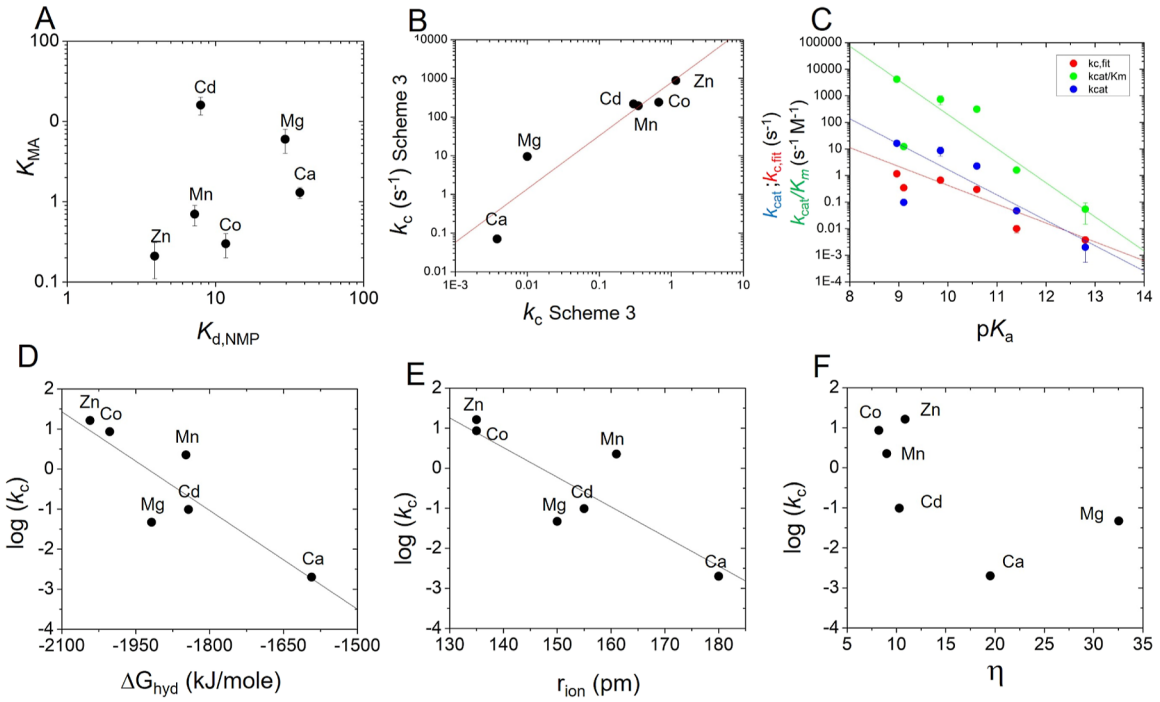

Figure 8. Analysis of k_c, the rate constant for catalysis the Psr metal complex (ES*M^{2+}). (A) Comparison of the affinity of divalent ions for nucleotide monophosphate ($K_{d,NMP}$) to the observed binding affinity of M_A (K_{MA}). The value of K_{MA} was determined by fitting the metal titration data, as shown in Figure 7. The lack of correlation reflects the apparent specificity of the Psr active site for different ions. The data for each ion are labeled. (B) Comparison of the k_c values determined by fitting the full metal ion titration datasets to Scheme 2 or estimated by fitting the data at limiting ion concentration according to Scheme 3. (C) Correlation between the pK_a of the metal aquo ion for each divalent metal ion versus the observed k_c/K_M (green, slope = 1.3), k_c estimated from fitting to Scheme 2 (red, slope = 0.71), and k_c estimated using k_c from Scheme 3 (blue, slope = 0.96). (D–F) Comparison of the potential correlations between log(k_c) and hydration free energy (ΔG_{hyd}), radius (r_{ion}), and absolute hardness (η) of divalent metal ions used. The data for log(k_c) versus hydration free energy and radius are fit to a linear function.

in its native context are missing, the observed thermal stability may be distinct from the full-length functional RNA, or simply sufficient to meet the requirements for its biological role. Since the Psr reaction in these studies is initiated by the addition of divalent ions, there are likely to be multiple interconverting conformational states during ion binding and adopting the reactive conformation. Differences in their thermodynamic properties may offset resulting in the observed temperature dependence.[49] Although the low T_m and minimal temperature dependence places a severe limit to achieving optimal catalytic activity, stabilizing the active conformation by engineering thermal stability based on the knowledge of structure and active site interactions can provide routes to optimization.

Psr likely Undergoes Interconversion between Local Conformational States with Varying Activity in a Metal-Dependent Fashion. Despite the rapid reaction rate, one key limiting factor is probably folding to the active conformation. SHAPE analysis of Psr equilibrium folding shows significant changes in reactivity at relatively low (5 mM) $MgCl_2$ concentration supporting local conformational changes induced by divalent ion binding.[33] Our results provide evidence for metal binding of similar affinity (~6 mM for Mg^{2+}) essential for Psr catalysis. FRET studies for the 8–17 DNAzyme show that a global folding occurs for various metal ions at concentrations lower than that required for cleavage activity, suggesting that the varying rate may be due to metal-dependent conformational changes.[58,59] Recent time-resolved NMR analysis of the dynamics associated with 10–23 DNAzyme catalysis showed how Mg^{2+} binding can alter active site conformations and distributions.[60] The hammerhead ribozyme (HHrz) has been shown to interconvert between conformational states with varying activity in a metal and pH-dependent fashion.[61,62] Additionally, other small ribozymes including HHrz and HDVrz can function in monovalent ions alone, and under these conditions, there is evidence that chemistry is rate-limiting. Therefore, it is possible that chemistry still could be rate-limiting for Psr, at least under certain conditions. Indeed, given the complex divalent metal ion dependence, low thermal stability, and precedent that these RNA-cleaving systems undergo metal-dependent local conformational changes correlated with activity, it is plausible that Psr has a similarly complex mechanistic landscape, the full extent of which remains to be characterized.

Analysis of Divalent Ion Dependence Enabled by Rapid Kinetics Permits Estimation of Relative Effects on Catalytic Rate (k_c). Within this complex landscape, a careful evaluation of divalent metal ion dependence including consideration of relative affinities and multiple activating or inhibiting binding sites is key. The divalent metal ion titration experiments, performed here under high monovalent ion conditions to fulfill diffuse metal ion requirements, provide evidence for a relatively high affinity, low specificity binding site for an activating, catalytic metal ion. Inhibitory effects at high concentrations >10 mM are accounted for by fitting the data to a two-metal ion binding model, or kinetic analyses under limiting ion concentrations. These analyses enable a more accurate estimation of k_c, supporting the previous observation of an inverse correlation between rate and the pK_a of the metal aquo ion. The relative magnitudes of the values of k_c estimated from fitting the full titration data

https://doi.org/10.1021/acs.biochem.3c00160
Biochemistry 2023, 62, 2079–2092

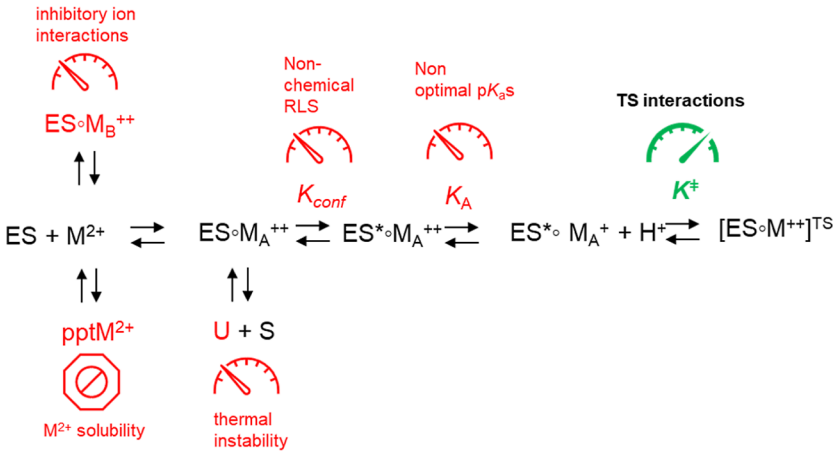

Figure 9. Factors that limit the ability of Psr to catalyze RNA 2′-*O*-transphosphorylation. A simple mechanistic model of the reaction of the Psr ES complex shows specific steps required to reach the transition state. The ES ground state ensemble is largely folded into the native structure and undergoes divalent metal ion binding (which may include inhibitory or anti-cooperative interactions), local conformational changes, active site ionization, and formation of interactions that provide $\alpha-\delta$ catalytic modes. Individual reaction steps can be subject to factors that limit their contribution to RNA strand cleavage, or which are amenable to further optimization as discussed in the text.

(Scheme 2) and by analyzing data at limiting metal ion concentration (Scheme 3) are similar and follow a linear relationship. Given the demonstrated influence of an inhibitory divalent ion binding site, the magnitude of k_c estimated from k_c/K_M measured at limiting concentration (0.96) is likely to be most accurate. The slope of $\log(k_c)$ versus pK_a interpreted at a mechanistic level places limits on potential catalytic roles. Thus, having accurate estimates of k_c provides critical benchmark data for validation of computational QM/MM studies that endeavor to determine reaction free energy surfaces and pathways that traverse through transition states with activation barriers that can be related to the intrinsic rates.[63]

Current Data Are Not Able to Definitively Confirm Mechanism but Support an Active Site Divalent Metal Ion in Psr likely to Act as a General Acid. It is important to fully consider the merits of different mechanistic alternatives in the context of a potentially complex reaction landscape. Like Psr, the 8−17 DNAzyme, 10−23 DNAzyme, and HHrz all also have rate constant increases with decreasing metal ion pK_a with slope near unity.[55,64−66] Simulations of different reaction states of 8−17 DNAzyme are consistent with inner-sphere coordination of the catalytic Pb^{2+} in the transition state to a non-bridging oxygen, as well as acting to stabilize the leaving group as a Lewis acid (primary δ-catalysis).[34] Like Psr, the fast rates achieved by 8−17 DNAzyme limit analysis of the cleavage reaction of the native enzyme. Recent kinetic studies of 8−17 DNAzyme bearing a G14 Ap modification to slow catalysis compared the pH rate profiles in Pb^{2+} (pK_a 7.8) versus Mg (pK_a 11.4). The results in this system reveal a higher pK_a for the catalytic acid in Mg^{2+} compared to Pb^{2+} consistent with metal ion water acting as an acid. The role of the divalent ion in HHrz is generally thought to be increasing the acidity of the 2′-OH of G8 (secondary δ catalysis), which is the functional group engaged in general acid (primary δ) catalysis. Alternatively, a metal-bound water has been suggested to act as a general acid.[67−69]

In the current model for Psr catalysis, the lower pK_a of a water molecule coordinated with the active site divalent ion provides more efficient proton transfer as a Brønsted acid in the transition state. The demonstrated importance of the active site metal ion by site modification, crystal structures showing the proximity of a divalent ion to the 5′O leaving group, and computational simulations starting from these structures support δ catalysis. In this regard, the interpretation of the observed slope of $\log(k_{obs})$ versus pK_a of 0.93 would reflect essentially complete proton transfer in the transition state. In this case, a significant solvent D_2O fractionation factor would be expected, which we do not observe. Instead, the minimal SKIE and temperature dependence demonstrated here suggest that a step, or steps, other than chemistry likely limit the reaction rate. However, the interpretation of a metal aquo ion acting in δ catalysis requires that the kinetics monitor the chemical transition state. A non-chemical rate-limiting step would likely mask a Brønsted signature for proton transfer in the transition state or potentially yield a break in the slope of the pK_a dependence. Additionally, the correlation between the apparent cleavage rate and divalent metal aquo ion pK_a must be accepted as the basis for the effect on catalysis, rather than related properties such as radius and polarizability, which could affect transition state stabilization. Recently, it was demonstrated that a 1-deazaguanine modification at G42 which should knock out the nucleophile activating general base showed no large effect.[42] This result was interpreted as showing minimal proton transfer prior to the rate-limiting transition state, or alternatively a nonchemical rate-limiting step. Either scenario is consistent with the lack of significant transition-state H/D fractionation. Thus, while current results are overall consistent with the interpretation that the metal aquo ion is serving as a general acid, it is important to note the potential for nonchemical steps limiting catalysis and kinetically indistinguishable mechanistic models.

Predictive Understanding of Psr Mechanism Will Aid in the Design of New Biotechnology and Therapeutics. Currently, the ribozymes that cut RNA can achieve $>10^6$-fold rate enhancement over spontaneous RNA 2′-*O*-transphosphorylation, but this remains orders of magnitude slower than protein ribonuclease.[16] The limitations of RNA catalysis for ribozymes and small-molecule catalysts can include limitations on flexibility, dynamics, mis-folding, limited population of correctly protonated active site residues, and the limited ability to employ multiple catalytic modes simultaneously (Figure 9).

https://doi.org/10.1021/acs.biochem.3c00160
Biochemistry 2023, 62, 2079−2092

Under optimal reaction conditions (Mg^{2+} concentration above 50 mM and pH between 7.5 and 9.0), the rate constant for Psr was projected to be ~1.7 s^{-1}. We measure k_c the rate constant for cleavage for the ribozyme Mg^{2+} complex to be within three-fold of this value at 0.6 s^{-1} at pH 8.0. Therefore, the catalytic step itself may be relatively well optimized with respect to catalytic modes in the transition state. The inclusion of high concentrations of monovalent ions to isolate the contribution of divalent ions here provides important insight into biophysical principles of functional ion binding. However, the results may not accurately reflect physiological ion binding due to the competition between monovalent and divalent ions, and the differential effects of monovalent ion types.[70] A limitation of the current study is that it does not explore the effects of varying monovalent ion identity and concentration (including K^+ ions and near-physiological concentrations). Hence, open questions remain as to the degree to which monovalent ion conditions give rise to the unusual thermal stability and reaction temperature dependence. This is an important question that will be the subject of a future work in order to fully explore. Indeed, a detailed study of the 10−23 DNAzyme showed that monovalent cations such as Na^+ or K^+ can have either activating or inhibitory effects on in vitro DNAzyme catalysis depending on the divalent metal ion employed,[70] resembling the apparent idiosyncratic effects for different metal ions observed here for Psr catalysis. Thus, interfering ion interactions can act as a barrier to optimal catalysis. Despite the ability of soft ions with low pK_a to facilitate rapid Psr kinetics, they are further limited to suboptimal pH ranges due to solubility. Another limitation of Psr catalysis, at least in the intermolecular construct examined here, is its instability at higher temperature (T_m of 42−45 °C) and broad unfolding transition beginning at ca. 25 °C. Understanding metal ion preferences and control of activity by temperature, ion identity, and pH are important for re-engineering naturally occurring ribozymes and artificial ribozymes and DNAzymes as programmable sensors and biotechnological tools. Moreover, the limitations to Psr catalysis identified here present potential challenges to overcome in the quest to understand the distinctions between ribozyme and ribonuclease catalysis.

Dramatic recent progress has revealed small endonucleolytic ribozyme and DNAzyme catalytic function in detail. Nonetheless, application to biotechnology and therapy is limited by insufficient understanding of the mechanistic factors that enable and constrain the catalytic function. Progress requires quantitative mechanistic investigation of the experimental details of structure−function relationships and careful consideration of the range of alternative mechanisms by modeling and simulation. These insights can prove useful in improving the activity and stability of ribozymes and DNAzymes for synthetic biology. Some of these limitations may be overcome by using non-natural nucleobases of alternative backbone architectures that enhance biological stability and avoid negative effects on binding specificity and divalent metal ion.[71−75] Optimization of endonucleolytic nucleic acids for diagnostic and therapeutic applications requires understanding the functional roles and specificities of metal-binding sites and their strong dependency on the scaffold provided by RNA structure and how they influence its dynamic behavior.

AUTHOR INFORMATION

Corresponding Author

Michael E. Harris − *Department of Chemistry, University of Florida, Gainesville, Florida 32611, United States;* orcid.org/0000-0001-8977-4392; Email: harris@chem.ufl.edu

Authors

Suhyun Yoon − *Department of Chemistry, University of Florida, Gainesville, Florida 32611, United States;* orcid.org/0000-0002-3764-0381

Edward Ollie − *Department of Chemistry, University of Florida, Gainesville, Florida 32611, United States*

Darrin M. York − *Department of Chemistry and Chemical Biology, Rutgers, The State University of New Jersey, Piscataway, New Jersey 08854, United States;* orcid.org/0000-0002-9193-7055

Joseph A. Piccirilli − *Department of Chemistry and Department of Biochemistry and Molecular Biology, The University of Chicago, Chicago, Illinois 60637, United States;* orcid.org/0000-0002-0541-6270

Complete contact information is available at: https://pubs.acs.org/10.1021/acs.biochem.3c00160

Notes

The authors declare no competing financial interest.

ACKNOWLEDGMENTS

The authors are grateful for the financial support provided by the National Institutes of Health (GM127100 to M.E.H., GM062248 to D.M.Y., and GM131568 to J.A.P.). The authors thank Prof. Şölen Ekesan for helpful discussions.

REFERENCES

(1) Peng, H.; Latifi, B.; Müller, S.; Lupták, A.; Chen, I. A. Self-cleaving ribozymes: substrate specificity and synthetic biology applications. *RSC Chem. Biol.* **2021**, *2*, 1370−1383.

(2) Jimenez, R. M.; Polanco, J. A.; Lupták, A. Chemistry and Biology of Self-Cleaving Ribozymes. *Trends Biochem. Sci.* **2015**, *40*, 648−661.

(3) Micura, R.; Höbartner, C. Fundamental studies of functional nucleic acids: aptamers, riboswitches, ribozymes and DNAzymes. *Chem. Soc. Rev.* **2020**, *49*, 7331−7353.

(4) Balke, D.; Hieronymus, R.; Müller, S. Challenges and Perspectives in Nucleic Acid Enzyme Engineering. *Adv. Biochem. Eng. Biotechnol.* **2020**, *170*, 21−35.

(5) Ren, A.; Micura, R.; Patel, D. J. Structure-based mechanistic insights into catalysis by small self-cleaving ribozymes. *Curr. Opin. Chem. Biol.* **2017**, *41*, 71−83.

(6) Seith, D. D.; Bingaman, J. L.; Veenis, A. J.; Button, A. C.; Bevilacqua, P. C. Elucidation of Catalytic Strategies of Small Nucleolytic Ribozymes From Comparative Analysis of Active Sites. *ACS Catal.* **2018**, *8*, 314−327.

(7) de la Peña, M.; García-Robles, I.; Cervera, A. The Hammerhead Ribozyme: A Long History for a Short RNA. *Molecules* **2017**, *22*, 78.

(8) Riccitelli, N.; Lupták, A. HDV family of self-cleaving ribozymes. *Prog. Mol. Biol. Transl. Sci.* **2013**, *120*, 123−171.

(9) Lilley, D. M. J. Classification of the nucleolytic ribozymes based upon catalytic mechanism. *F1000Research* **2019**, *8*, 1462.

(10) Lilley, D. M. J. How RNA acts as a nuclease: some mechanistic comparisons in the nucleolytic ribozymes. *Biochem. Soc. Trans.* **2017**, *45*, 683−691.

(11) DasGupta, S.; Piccirilli, J. A. The Varkud Satellite Ribozyme: A Thirty-Year Journey through Biochemistry, Crystallography, and Computation. *Acc. Chem. Res.* **2021**, *54*, 2591−2602.

(12) Ganguly, A.; Weissman, B. P.; Giese, T. J.; Li, N. S.; Hoshika, S.; Rao, S.; Benner, S. A.; Piccirilli, J. A.; York, D. M. Confluence of theory and experiment reveals the catalytic mechanism of the Varkud satellite ribozyme. *Nat. Chem.* **2020**, *12*, 193−201.
(13) Ganguly, A.; Weissman, B. P.; Piccirilli, J. A.; York, D. M. Evidence for a Catalytic Strategy to Promote Nucleophile Activation in Metal-Dependent RNA-Cleaving Ribozymes and 8-17 DNAzyme. *ACS Catal.* **2019**, *9*, 10612−10617.
(14) Kostenbader, K.; York, D. M. Molecular simulations of the pistol ribozyme: unifying the interpretation of experimental data and establishing functional links with the hammerhead ribozyme. *RNA* **2019**, *25*, 1439−1456.
(15) Gaines, C. S.; Giese, T. J.; York, D. M. Cleaning Up Mechanistic Debris Generated by Twister Ribozymes Using Computational RNA Enzymology. *ACS Catal.* **2019**, *9*, 5803−5815.
(16) Emilsson, G. M.; Nakamura, S.; Roth, A.; Breaker, R. R. Ribozyme speed limits. *RNA* **2003**, *9*, 907−918.
(17) Bevilacqua, P. C.; Harris, M. E.; Piccirilli, J. A.; Gaines, C.; Ganguly, A.; Kostenbader, K.; Ekesan, S.; York, D. M. An Ontology for Facilitating Discussion of Catalytic Strategies of RNA-Cleaving Enzymes. *ACS Chem. Biol.* **2019**, *14*, 1068−1076.
(18) Gaines, C. S.; Piccirilli, J. A.; York, D. M. The L-platform/L-scaffold framework: a blueprint for RNA-cleaving nucleic acid enzyme design. *RNA* **2020**, *26*, 111−125.
(19) Mikkola, S.; Lönnberg, T.; Lönnberg, H. Phosphodiester models for cleavage of nucleic acids. *Beilstein J. Org. Chem.* **2018**, *14*, 803−837.
(20) Lonnberg, H. Isomerization of RNA Phosphodiester Linkages. In *Chemical Biology of the Nucleic Acids*; Erdmann, V. A., Markiewicz, W. T., Barciszewski, J., Eds., Springer Berlin, Heidelberg, 2014.
(21) Oivanen, M.; Kuusela, S.; Lonnberg, H. Kinetics and mechanisms for the cleavage and isomerization of the phosphodiester bonds of RNA by Bronsted acids and bases. *Chem. Rev.* **1998**, *98*, 961−990.
(22) Gu, H.; Zhang, S.; Wong, K. Y.; Radak, B. K.; Dissanayake, T.; Kellerman, D. L.; Dai, Q.; Miyagi, M.; Anderson, V. E.; York, D. M.; Piccirilli, J. A.; Harris, M. E. Experimental and computational analysis of the transition state for ribonuclease A-catalyzed RNA 2'-O-transphosphorylation. *Proc. Natl. Acad. Sci. U.S.A.* **2013**, *110*, 13002−13007.
(23) Weissman, B.; Ekesan, Ş.; Lin, H. C.; Gardezi, S.; Li, N. S.; Giese, T. J.; McCarthy, E.; Harris, M. E.; York, D. M.; Piccirilli, J. A. Dissociative Transition State in Hepatitis Delta Virus Ribozyme Catalysis. *J. Am. Chem. Soc.* **2023**, *145*, 2830−2839.
(24) Wilson, T. J.; Lilley, D. M. J. *The Potential Versatility of RNA Catalysis*; Wiley Interdiscip Rev RNA, 2021; Vol. *12*, p e1651.
(25) Peng, H.; Latifi, B.; Müller, S.; Lupták, A.; Chen, I. A. Self-cleaving ribozymes: substrate specificity and synthetic biology applications. *RSC Chem. Biol.* **2021**, *2*, 1370−1383.
(26) Harris, K. A.; Lünse, C. E.; Li, S.; Brewer, K. I.; Breaker, R. R. Biochemical analysis of pistol self-cleaving ribozymes. *RNA* **2015**, *21*, 1852−1858.
(27) Weinberg, Z.; Kim, P. B.; Chen, T. H.; Li, S.; Harris, K. A.; Lunse, C. E.; Breaker, R. R. New classes of self-cleaving ribozymes revealed by comparative genomics analysis. *Nat. Chem. Biol.* **2015**, *11*, 606−610.
(28) Weinberg, Z.; Kim, P. B.; Chen, T. H.; Li, S.; Harris, K. A.; Lünse, C. E.; Breaker, R. R. New classes of self-cleaving ribozymes revealed by comparative genomics analysis. *Nat. Chem. Biol.* **2015**, *11*, 606−610.
(29) Ren, A.; Vušurović, N.; Gebetsberger, J.; Gao, P.; Juen, M.; Kreutz, C.; Micura, R.; Patel, D. J. Pistol ribozyme adopts a pseudoknot fold facilitating site-specific in-line cleavage. *Nat. Chem. Biol.* **2016**, *12*, 702−708.
(30) Nguyen, L. A.; Wang, J.; Steitz, T. A. Crystal structure of Pistol, a class of self-cleaving ribozyme. *Proc. Natl. Acad. Sci. U.S.A.* **2017**, *114*, 1021−1026.
(31) Teplova, M.; Falschlunger, C.; Krasheninina, O.; Egger, M.; Ren, A.; Patel, D. J.; Micura, R. Crucial Roles of Two Hydrated Mg(2+) Ions in Reaction Catalysis of the Pistol Ribozyme. *Angew Chem. Int. Ed. Engl.* **2020**, *59*, 2837−2843.
(32) Wilson, T. J.; Liu, Y.; Li, N. S.; Dai, Q.; Piccirilli, J. A.; Lilley, D. M. J. Comparison of the Structures and Mechanisms of the Pistol and Hammerhead Ribozymes. *J. Am. Chem. Soc.* **2019**, *141*, 7865−7875.
(33) Gasser, C.; Gebetsberger, J.; Gebetsberger, M.; Micura, R. SHAPE probing pictures Mg2+-dependent folding of small self-cleaving ribozymes. *Nucleic Acids Res.* **2018**, *46*, 6983−6995.
(34) Ekesan, Ş.; York, D. M. Dynamical ensemble of the active state and transition state mimic for the RNA-cleaving 8-17 DNAzyme in solution. *Nucleic Acids Res.* **2019**, *47*, 10282−10295.
(35) Weinberg, C. E.; Weinberg, Z.; Hammann, C. Novel ribozymes: discovery, catalytic mechanisms, and the quest to understand biological function. *Nucleic Acids Res.* **2019**, *47*, 9480−9494.
(36) Ekesan, Ş.; York, D. M. Who stole the proton? Suspect general base guanine found with a smoking gun in the pistol ribozyme. *Org. Biomol. Chem.* **2022**, *20*, 6219−6230.
(37) Neuner, S.; Falschlunger, C.; Fuchs, E.; Himmelstoss, M.; Ren, A.; Patel, D. J.; Micura, R. Atom-Specific Mutagenesis Reveals Structural and Catalytic Roles for an Active-Site Adenosine and Hydrated Mg(2+) in Pistol Ribozymes. *Angew Chem. Int. Ed. Engl.* **2017**, *56*, 15954−15958.
(38) Lihanova, Y.; Weinberg, C. E. Biochemical analysis of cleavage and ligation activities of the pistol ribozyme from Paenibacillus polymyxa. *RNA Biol.* **2021**, *18*, 1858−1866.
(39) Leamy, K. A.; Yennawar, N. H.; Bevilacqua, P. C. Cooperative RNA Folding under Cellular Conditions Arises From Both Tertiary Structure Stabilization and Secondary Structure Destabilization. *Biochemistry* **2017**, *56*, 3422−3433.
(40) Chadalavada, D. M.; Cerrone-Szakal, A. L.; Wilcox, J. L.; Siegfried, N. A.; Bevilacqua, P. C. Mechanistic analysis of the hepatitis delta virus (HDV) ribozyme: methods for RNA preparation, structure mapping, solvent isotope effects, and co-transcriptional cleavage. *Methods Mol. Biol.* **2012**, *848*, 21−40.
(41) Bevilacqua, P. C. Mechanistic considerations for general acid-base catalysis by RNA: revisiting the mechanism of the hairpin ribozyme. *Biochemistry* **2003**, *42*, 2259−2265.
(42) Egger, M.; Bereiter, R.; Mair, S.; Micura, R. Scaling Catalytic Contributions of Small Self-Cleaving Ribozymes. *Angew Chem. Int. Ed. Engl.* **2022**, *61*, No. e202207590.
(43) Draper, D. E. A guide to ions and RNA structure. *RNA* **2004**, *10*, 335−343.
(44) Todisco, M.; Szostak, J. W. Hybridization kinetics of out-of-equilibrium mixtures of short RNA oligonucleotides. *Nucleic Acids Res.* **2022**, *50*, 9647−9662.
(45) Gray, D. M.; Hung, S.-H.; Johnson, K. H. Absorption and circular dichroism spectroscopy of nucleic acid duplexes and triplexes. *Methods Enzymol.* **1995**, *246*, 19−34.
(46) Sosnick, T. R.; Fang, X.; Shelton, V. M. Application of circular dichroism to study RNA folding transitions. *Methods Enzymol.* **2000**, *317*, 393−409.
(47) Akoopie, A.; Müller, U. F. Lower temperature optimum of a smaller, fragmented triphosphorylation ribozyme. *Phys. Chem. Chem. Phys.* **2016**, *18*, 20118−20125.
(48) Li, Y.; Breaker, R. R. Kinetics of RNA Degradation by Specific Base Catalysis of Transesterification Involving the 2′-Hydroxyl Group. *J. Am. Chem. Soc.* **1999**, *121*, 5364−5372.
(49) Peracchi, A. Origins of the temperature dependence of hammerhead ribozyme catalysis. *Nucleic Acids Res.* **1999**, *27*, 2875−2882.
(50) Takagi, Y.; Taira, K. Temperature-dependent change in the rate-determining step in a reaction catalyzed by a hammerhead ribozyme. *FEBS Lett.* **1995**, *361*, 273−276.
(51) Izatt, R. M.; Christensen, J. J.; Rytting, J. H. Sites and thermodynamic quantities associated with proton and metal ion interaction with ribonucleic acid, deoxyribonucleic acid, and their constituent bases, nucleosides, and and nucleotides. *Chem. Rev.* **1971**, *71*, 439−481.

https://doi.org/10.1021/acs.biochem.3c00160
Biochemistry 2023, 62, 2079−2092

(52) Schowen, K. B.; Schowen, R. L. Solvent isotope effects of enzyme systems. *Methods Enzymol.* **1982**, *87*, 551−606.
(53) Quinn, D. Theory and Practice of Solvent Isotope Effects. In *Isotope Effects in Chemistry and Biology*; Kohen, A., Limbach, H.-H., Eds., CRC Press, Boca Raton, 2005; pp 995−1018.
(54) Fernandez, P. L.; Murkin, A. S. Inverse Solvent Isotope Effects in Enzyme-Catalyzed Reactions. *Molecules* **2020**, *25*, 1933.
(55) Bonaccio, M.; Credali, A.; Peracchi, A. Kinetic and thermodynamic characterization of the RNA-cleaving 8-17 deoxyribozyme. *Nucleic Acids Res.* **2004**, *32*, 916−925.
(56) White, N. A.; Hoogstraten, C. G. Thermodynamics and kinetics of RNA tertiary structure formation in the junctionless hairpin ribozyme. *Biophys. Chem.* **2017**, *228*, 62−68.
(57) Li, Y.; Bevilacqua, P. C.; Mathews, D.; Turner, D. H. Thermodynamic and activation parameters for binding of a pyrene-labeled substrate by the Tetrahymena ribozyme: docking is not diffusion-controlled and is driven by a favorable entropy change. *Biochemistry* **1995**, *34*, 14394−14399.
(58) Kim, H.-K.; Liu, J.; Li, J.; Nagraj, N.; Li, M.; Pavot, C. M. B.; Lu, Y. Metal-Dependent Global Folding and Activity of the 8-17 DNAzyme Studied by Fluorescence Resonance Energy Transfer. *J. Am. Chem. Soc.* **2007**, *129*, 6896−6902.
(59) Mazumdar, D.; Nagraj, N.; Kim, H.-K.; Meng, X.; Brown, A. K.; Sun, Q.; Li, W.; Lu, Y. Activity, Folding and Z-DNA Formation of the 8-17 DNAzyme in the Presence of Monovalent Ions. *J. Am. Chem. Soc.* **2009**, *131*, 5506−5515.
(60) Borggräfe, J.; Victor, J.; Rosenbach, H.; Viegas, A.; Gertzen, C. G. W.; Wuebben, C.; Kovacs, H.; Gopalswamy, M.; Riesner, D.; Steger, G.; Schiemann, O.; Gohlke, H.; Span, I.; et al. Time-resolved structural analysis of an RNA-cleaving DNA catalyst. *Nature* **2022**, *601*, 144−149.
(61) Murray, J. B.; Dunham, C. M.; Scott, W. G. A pH-dependent conformational change, rather than the chemical step, appears to be rate-limiting in the hammerhead ribozyme cleavage reaction 1 1Edited by J. Doudna. *J. Mol. Biol.* **2002**, *315*, 121−130.
(62) Hammann, C.; Norman, D. G.; Lilley, D. M. Dissection of the ion-induced folding of the hammerhead ribozyme using 19F NMR. *Proc. Natl. Acad. Sci. U.S.A.* **2001**, *98*, 5503−5508.
(63) Garcia-Viloca, M.; Gao, J.; Karplus, M.; Truhlar, D. G. How Enzymes Work: Analysis by Modern Rate Theory and Computer Simulations. *Science* **2004**, *303*, 186−195.
(64) Dahm, S. C.; Derrick, W. B.; Uhlenbeck, O. C. Evidence for the role of solvated metal hydroxide in the hammerhead cleavage mechanism. *Biochemistry* **1993**, *32*, 13040−13045.
(65) Roychowdhury-Saha, M.; Burke, D. H. Extraordinary rates of transition metal ion-mediated ribozyme catalysis. *RNA* **2006**, *12*, 1846−1852.
(66) Santoro, S. W.; Joyce, G. F. Mechanism and Utility of an RNA-Cleaving DNA Enzyme. *Biochemistry* **1998**, *37*, 13330−13342.
(67) Ward, W. L.; Plakos, K.; DeRose, V. J. Nucleic Acid Catalysis: Metals, Nucleobases, and Other Cofactors. *Chem. Rev.* **2014**, *114*, 4318−4342.
(68) Mir, A.; Chen, J.; Robinson, K.; Lendy, E.; Goodman, J.; Neau, D.; Golden, B. L. Two Divalent Metal Ions and Conformational Changes Play Roles in the Hammerhead Ribozyme Cleavage Reaction. *Biochemistry* **2015**, *54*, 6369−6381.
(69) Ward, W. L.; Derose, V. J. Ground-state coordination of a catalytic metal to the scissile phosphate of a tertiary-stabilized Hammerhead ribozyme. *RNA* **2012**, *18*, 16−23.
(70) Rosenbach, H.; Borggräfe, J.; Victor, J.; Wuebben, C.; Schiemann, O.; Hoyer, W.; Steger, G.; Etzkorn, M.; Span, I. Influence of monovalent metal ions on metal binding and catalytic activity of the 10-23 DNAzyme. *Biol. Chem.* **2020**, *402*, 99−111.
(71) Wang, Y.; Nguyen, K.; Spitale, R. C.; Chaput, J. C. A biologically stable DNAzyme that efficiently silences gene expression in cells. *Nat. Chem.* **2021**, *13*, 319−326.
(72) Chaput, J. C. Redesigning the Genetic Polymers of Life. *Acc. Chem. Res.* **2021**, *54*, 1056−1065.
(73) Wang, Y.; Liu, E.; Lam, C. H.; Perrin, D. M. A densely modified M(2+)-independent DNAzyme that cleaves RNA efficiently with multiple catalytic turnover. *Chem. Sci.* **2018**, *9*, 1813−1821.
(74) Jerome, C. A.; Hoshika, S.; Bradley, K. M.; Benner, S. A.; Biondi, E. In vitro evolution of ribonucleases from expanded genetic alphabets. *Proc. Natl. Acad. Sci. U.S.A.* **2022**, *119*, No. e2208261119.
(75) Hoshika, S.; Leal, N. A.; Kim, M. J.; Kim, M. S.; Karalkar, N. B.; Kim, H. J.; Bates, A. M.; Watkins, N. E., Jr.; SantaLucia, H. A.; Meyer, A. J.; DasGupta, S.; Piccirilli, J. A.; Ellington, A. D.; SantaLucia, J., Jr.; Georgiadis, M. M.; Benner, S. A. Hachimoji DNA and RNA: A genetic system with eight building blocks. *Science* **2019**, *363*, 884−887.

https://doi.org/10.1021/acs.biochem.3c00160
Biochemistry 2023, 62, 2079−2092